# Hydrogen permeation from F82H wall of ceramic breeder pebble bed: The effect of surface corrosion

Keisuke Mukai,[a*] Shunsuke Kenjo,[b] Naoto Iwamatsu,[b] Bakr Mahmoud,[a,c] Takumi Chikada,[d] Juro Yagi,[a] Satoshi Konishi[a]

[a] Institute of Advanced Energy, Kyoto University, Gokasho, Uji, Kyoto 611-0011, Japan

[b] Graduate School of Energy Science, Kyoto University, Uji, Kyoto 611-0011, Japan

[c] Physics Department, Faculty of Science, Assiut University, Assiut 71516, Egypt

[d] Graduate School of Integral Science and Technology, Shizuoka University, 836 Ohya Suruga-ku, Shizuoka 422-8529, Japan

*Corresponding author: k-mukai@iae.kyoto-u.ac.jp Tel: +81774-38-3432, FAX: +81774-38-34399

## Highlights

- ✓ In-situ hydrogen permeation test from F82H wall of LTZO ceramic breeder pebble bed
- ✓ Surface corrosion oxide layers on RAFM F82H steel reduced hydrogen permeation
- ✓ The corrosion layer achieved permeation reduction factors of 20–50 at 598 K
- ✓ The activation energies of hydrogen permeation were 0.65–0.78 eV
- ✓ The layers showed a thermal stability with a possible self-repairing ability

## Abstract

Understanding the permeation behavior of tritium from a pebble bed breeding blanket is essential for establishing a self-sufficient fuel cycle in a nuclear fusion reactor. It is known that double corrosion layers forms on reduced activation ferritic-martensitic (RAFM) steel surface by gas release from a ceramic breeder material, however, its effect on hydrogen permeation behavior has not been elucidated. Herein, in-situ measurement of hydrogen permeation through an F82H RAFM wall of a ceramic breeder pebble bed was performed under $H_2$-added sweep gas conditions. The corrosion layer formed on the F82H sample had a dense microstructure, which reduced hydrogen permeation flux at least by one order of magnitude. The permeation reduction factors were 20–50 at the water-coolant temperature of a blanket. A self-repairing ability is expected for the surface oxide layer as the corrosion occurs spontaneously inside a breeding blanket.

# 1. Introduction

Nuclear fusion is a sustainable and low-carbon energy source with a self-sufficient hydrogen isotope fuel system. A solid breeding blanket concept has been developed for future implementation in a demonstration fusion reactor [1,2], in which the fuel tritium is produced by ceramic breeder pebbles (lithium oxides) using neutron capture by Li (i.e., $^6Li + {}^1n \rightarrow {}^3T + {}^4He$). Bred tritium is recovered by $H_2$-added sweep gas and utilized as a fuel for deuterium–tritium fusion plasma. Tritium permeation through the blanket structural material, i.e., reduced activation ferritic martensitic (RAFM) steel, is a key issue because of (1) loss of the fuel tritium and (2) migration of radioactive tritium into the coolant. Reportedly, approximately 1% of the produced tritium is lost from a breeding blankets by permeation [3]. Hydrogen permeation barrier coatings have been developed to reduce the permeation significantly [4–10]. Typical permeation reduction factors (PRFs) for ceramic coatings with thickness of ~1 μm are 10 (TiC) [11], 100 (BN and TiN) [12], 1000 ($ZrO_2$, $Al_2O_3$, $Y_2O_3$, and $Er_2O_3$) [13–16] and 4600 (ZrN) [17] where their performance strongly depends on the microstructure as well as the thickness. The PRF can be further improved by a both-side coating [16] and a multi-layer coating [18]. A self-repairing ability is reported for $Y_2O_3$ stabilized $ZrO_2$ coating [19]. Nevertheless, a surface coating process inevitably imposes an extra cost in manufacturing of breeding blankets.

The surface of an RAFM steel is corroded by ceramic breeder materials (e.g., $Li_2TiO_3$ and $Li_4SiO_4$) at elevated temperatures because of the release of corrosive gas species, which forms multiple oxide layers on RAFM steels [20–24] and consequently reduces the fatigue lifetime [25]. The growth of the corrosion layer is controlled by the diffusion process and significantly affected by the moisture concentration as shown in our previous experiments [22–24]. Even if an RAFM steel is coated with oxides, they are gradually corroded by diffusions of $Li^+$ and $O^{2-}$ into the coatings [26,27]. To date, very limited numbers of studies have investigated the effect of corrosion on hydrogen permeation behavior. Previously, deuterium permeation through the oxide layer formed on F82H RAFM steel heated in He + 1% $H_2$ atmosphere was investigated; however, the permeation was not clearly suppressed at >573 K [28]. In contrast, the corrosion of CLF-1 RAFM steel samples by $Li_4SiO_4$ powder in air reportedly reduced hydrogen permeation by approximately one order of magnitude [29]. However, the ability and stability of the corrosion layers formed on the RAFM surface to reduce tritium permeation remains unclear. As the corrosion layer is generally fragile, hydrogen permeation may be affected by microscopic cracks initiated during sample loading for a permeation test. Additionally, another cause that may affect permeation behavior is the reduction of the corrosion oxide layer during a permeation test in a strongly reducing $H_2$ atmosphere, as reported previously [28]. Thus, in this study, in-situ measurement of hydrogen permeation from a pebble bed was performed to elucidate the effects of corrosion under a sweep gas atmosphere. To observe this, the F82H RAFM steel sample was corroded by solid-solution pebbles of $Li_{2+x}TiO_{3+y}$ with $Li_2ZrO_3$ (LTZO) at 773 K as

an acceleration condition in sweep-gas-relevant atmospheres, while hydrogen permeabilities were measured at 623–773 K. After the test, glow-discharge optical emission spectroscopy (GD-OES) was employed to assess the element depth profiles including low $Z$ elements (i.e. H and Li) in the F82H samples.

## 2. Methods

### 2.1 Hydrogen permeation test

The F82H BA07-heat produced by vacuum induction melting followed by electroslag remelting was supplied from the National Institutes for Quantum Science and Technology (QST) [30]. The chemical composition (wt%) of the F82H BA07-heat was Fe, 7.97% Cr, 1.88% W, 0.45% Mn, 0.19% V, and 0.088% C [31]. The rectangular ingot was cut into a disk with thickness ~0.5 mm and diameter ~20 mm. Both sides of the F82H samples were mirror-polished. LTZO pebbles fabricated using the emulsion method were supplied from QST [32]. The pebbles had a Li excessive composition with a Li/Ti ratio of 2.15 [32]. The average diameter of the pebbles was approximately 1.1 mm. The pebbles were dried at 623 K for 5 h under vacuum (<$10^{-2}$ Pa). During the dry process, gas analysis was carried out using a quadrupole mass spectrometer (QMS, Canon Anelva Corp. M-101QA-TDF), which confirmed release of the gas species with mass numbers of 18 and 44, corresponding to $H_2O$ and $CO_2$ respectively.

Fig. 1 shows the experimental setup for the hydrogen permeation test. On the upper side, gas was continuously supplied to the stainless double tube at atmospheric pressure with a flow rate of 20 $cm^3$/min. The gas was dried using a molecular sieve column. Lower side was pumped by a rotary pump and turbo molecular pumps, in which the hydrogen isotopes permeated through the F82H samples were measured by the QMS. First, hydrogen permeation through the bare F82H sample was measured under Ar + 0.1% $H_2$, Ar + 1.0% $H_2$, $H_2$, and $D_2$ gas flow conditions. Second, hydrogen permeation tests were carried out with the dried LTZO pebbles (approximately 5 g) packed on the F82H sample under Ar + 0.1% $H_2$ and Ar + 1.0% $H_2$ gas flow conditions. The humidity of the outlet gas was monitored using a dew-point meter. The temperature monitored by the thermocouple placed in contact with the outer tube on the lower side (Fig. 1) was referred to as the sample temperature $T$, while temperature monitored by the thermocouple attached to the electric furnace was heater temperature $T_h$. $T$ was higher than $T_h$ by approximately 15 K. After the heater temperature reached to $T_h$ = 773 K, it was maintained for 72 h. Then, it was altered to 728, 688, 653, and 623 K. At each temperature drop, the heater temperature kept constant for 4 h to obtain a stable value of the ion current by the QMS. The heater temperature was again elevated to 773 K and kept constant for 144 h. Thereafter, the heater temperature was dropped with the same temperature step. The ion current measured by the QMS at the first and second temperature steps are called as data 1 and data 2,

respectively. Finally, the heater was cooled to room temperature by natural cooling.

The hydrogen permeation flux at steady state $J$ (mol m$^{-2}$ s$^{-1}$) through a material with thickness $d$ (m) is expressed as follows:

$$J = P \frac{p^n}{d} \tag{1}$$

where $P$, $p$, and $n$ are permeability (mol m$^{-1}$ s$^{-1}$ Pa$^{-n}$), driving pressure (Pa), and the pressure exponent, respectively. The exponent $n$ equals 0.5 when the permeation is controlled by the diffusion process, while the exponent approaches 1.0 when the surface reaction is the rate limiting process. The hydrogen permeation flux $J$ was obtained from ion intensity for mass number 2, $I$ (A), as follows:

$$J = k \frac{I - I_{BKG}}{A} \tag{2}$$

where $k$, $A$, and $I_{BKG}$ are the calibration factor (mol s$^{-1}$ A$^{-1}$), the area for the permeation (m$^2$), and the ion current of the background for mass number 2 (A). The activation energy of permeation was obtained from the slope of the permeation flux in the Arrhenius plot. The calibration factor $k$ (mol s$^{-1}$ A$^{-1}$) was obtained by integrating the total H$_2$ release from 37 mg (0.742 mmol) of TiH$_2$ powder. As a result, $k$ was obtained to be 36.5 mol s$^{-1}$ A$^{-1}$ with an error of <3%. The ion currents at room temperature after the permeation tests were used as $I_{BKG}$. The average values of the ion currents and their standard deviation were obtained from 50 data points measured by the QMS. PRF is defined as the permeation flux from the bare F82H sample divided by the corroded F82H sample, in this paper.
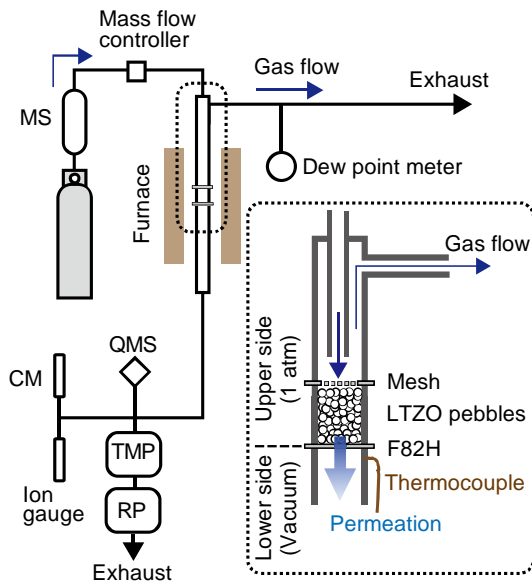


Fig. 1 Schematic diagram of the experimental setup, wherein MS, QMS, TMP, RP, and CM denote molecular sieve, quadrupole mass spectrometer, turbo molecular pump, rotary pump, and capacitance manometer, respectively.

## 2.2 Characterizations

X-ray diffraction (XRD) was carried out with a RINT TTR-III (Rigaku) using Co–$K\alpha$ radiation in the $2\theta$ range from 15 to 80$^\circ$ at intervals of 0.02$^\circ$ step. Both sides of the F82H sample after the permeation test were investigated using XRD. The LTZO pebbles were crushed into powder using an agate mortar for XRD measurements. Theoretical XRD patterns were simulated using VESTA software [33]. The surfaces of the F82H samples in contact with the LTZO pebbles were observed by field emission scanning electron microscope (SEM, Zeiss Ultra 55). Depth profiles of the F82H samples were investigated using GD-OES with a GD Profiler 2 (Horiba Ltd.). The diameter of hole created by Ar sputtering was approximately 4 mm. The depths of the holes were measured using atomic force microscopy (AFM, VN8010 KEYENCE. Co.). The sputtering rate of the corroded F82H sample was estimated to be 67 $\mu$m/s with an uncertainty of 10%, based on the surface roughness of the corroded sample.

## Results and discussion

### 3.1 Hydrogen permeation

First, hydrogen permeation through the bare F82H sample was investigated under Ar + 0.1% $H_2$, Ar + 1.0% $H_2$, $H_2$, and $D_2$ gas flow conditions. Fig. 2 shows the hydrogen isotope permeation fluxes plotted with the driving pressure and inverse temperature. In Fig. 2a, as a result of fittings of the data by power approximation, the exponents ($n$) for the three different driving pressures were estimated to be $n = 0.63$–0.70. The slopes for the two data at the low driving pressures (i.e. $1.01 \times 10^2$ and $1.01 \times 10^3$ Pa) were steeper than those for $1.01 \times 10^3$ and $1.01 \times 10^5$ Pa (Fig. 2a). Such a change in the rate-limiting process in a low driving pressure range was also observed in the previous work [14]. This indicates that the surface effects such as recombination and adsorption cannot be neglected for the $H_2$-added sweep gas conditions with low hydrogen partial pressures. Thus, in the following analysis, the data are represented as the permeation flux. Nevertheless, the hydrogen and deuterium permeabilities measured under $H_2$ and $D_2$ conditions were confirmed to be comparable with the previous data [34,35], by assuming the diffusion control regime ($n = 0.5$). As shown in Fig. 2b, the measured permeation fluxes linearly decreased with the inverse temperature in the Arrhenius plot. From the slopes of the fitting lines, the activation energies of permeation for the bare F82H in Ar + 0.1% $H_2$, Ar + 1.0% $H_2$, $H_2$, and $D_2$ gas were estimated to be 0.43(4), 0.463(3), 0.439(2), and 0.45(2) eV, respectively. These values agree well with the previously reported activation energies for the bare F82H (0.42–0.47 eV) [35]. The isotope effect of hydrogen and deuterium on the permeability flux, $J_D/J_H$, was estimated to be ~1.37, in consistent with the previously reported ratio of ~1.4 [36].
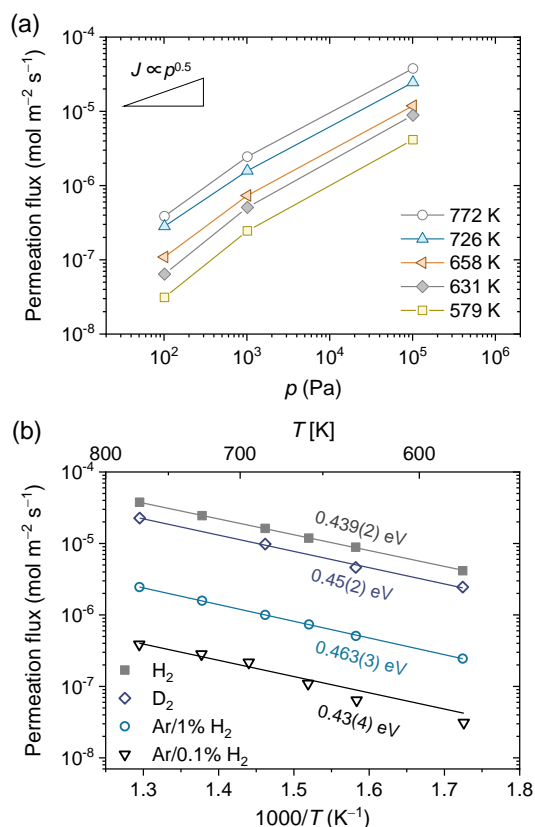
Fig. 2 Permeation flux of hydrogen isotopes through the bare F82H sample plotted with (a) the driving pressure $p$ and (b) inverse temperature. In panel (a), each data point is connected by lines. In panel (b), numbers in unit of eV represent the activation energies of permeation.

Fig. 3 shows the temporal changes in the ion current for mass number 2 (i.e. $H_2$), $I$, during the permeation tests under the Ar + 0.1% $H_2$ and Ar + 1.0% $H_2$ gas flow conditions. During the tests, the moisture concentrations were in the range of 100–300 ppmv, although it increased to 500 ppmv in the initial temperature elevation from a room temperature to $T_h$ = 773 K. Even during the initial heating, the ion current values did not reach the levels of $I$ obtained with the bare F82H sample. This indicates that gas release from the LTZO pebbles during the initial heating period resulted in the formation of oxide layers on the F82H samples, which readily suppressed hydrogen permeation. In this moisture range, the gas phase of LiOH is a dominant corrosive gas, based on the previous thermochemical analysis of $Li_{2.12(2)}TiO_{3+y}$ [37]. The ion current after the initial heating gradually decreased with the growth of the oxide layer on the F82H samples. The horizontal dotted line in Fig.3 shows that the ion current values before and after the first temperature step for data 1 were nearly unchanged, indicating a negligible impact of the oxide layer growth during the temperature step. The line also indicates that hydrogen permeation flux gradually decreased in the period between data 1 and data 2, although the decreasing rates were obviously slower than the first 72 h. The ion current decreased with temperature

in both periods for data 1 and data 2 where no sudden change in $I$, typically caused by peel-off or microcrack initiation of the surface oxide layer, was observed.
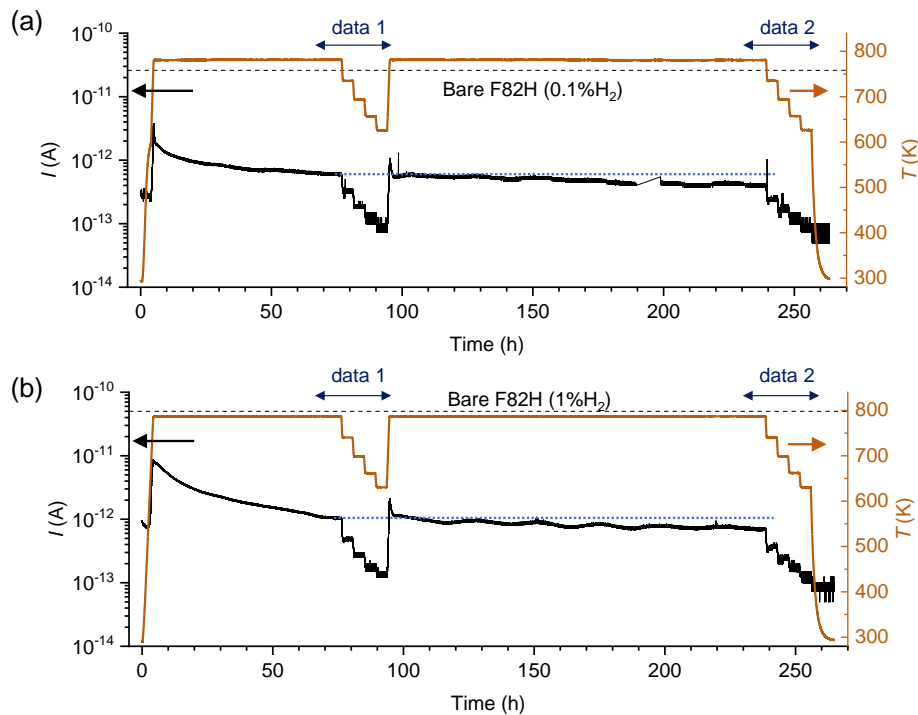


Fig. 3 Ion current $I$ (left axis) of mass 2 ($H_2$) measured by the quadrupole mass spectrometer under the (a) Ar + 0.1% $H_2$ and (b) Ar + 1.0% $H_2$ conditions represented with sample temperature $T$ (right axis). Horizontal broken line denotes ion current of mass 2 measured with the bare F82H sample. Horizontal dotted line indicates that the changes in $I$ after the temperature change for data 1 were negligibly small.

The Arrhenius plots of the hydrogen permeation fluxes are shown in Fig. 4. The reductions of hydrogen permeation in data 2 were clearly observed at $T_h$ = 728 and 667 K, while the difference was hindered by the large standard deviations at lower temperatures. In data 2, $I$ at $T_h$ = 773 K decreased by 31% (Ar + 0.1%) and 36% (Ar + 1.0%) from data 1, which could be explained by an increase in the diffusion distance associated with the growth of the corrosion layer. From the slopes of the exponential fittings, the activation energies of permeation for data 1 and data 2 in Ar + 0.1% $H_2$ gas flow condition were obtained to be 0.76(2) and 0.65(1) eV, respectively. In Ar + 1.0% $H_2$, the activation energies for data 1 and data 2 were 0.78(2) and 0.73(2) eV, respectively. The differences between the activation energies obtained from data 1 and data 2, for both the conditions, were insignificant. This is because the energy barriers for hydrogen diffusion and solution are independent on the thickness of the corrosion layers. The activation energies of the corroded sample increased from 0.2 to 0.3 eV

compared with the results with the bare F82H. The activation energies for the corroded F82H samples are comparable with those of RAFM steels coated with $ZrO_2$ (0.73(9) eV) [13], $Y_2O_3$ (0.70(2) eV) [15], and $Er_2O_3$ (0.62–0.63 eV) [16].
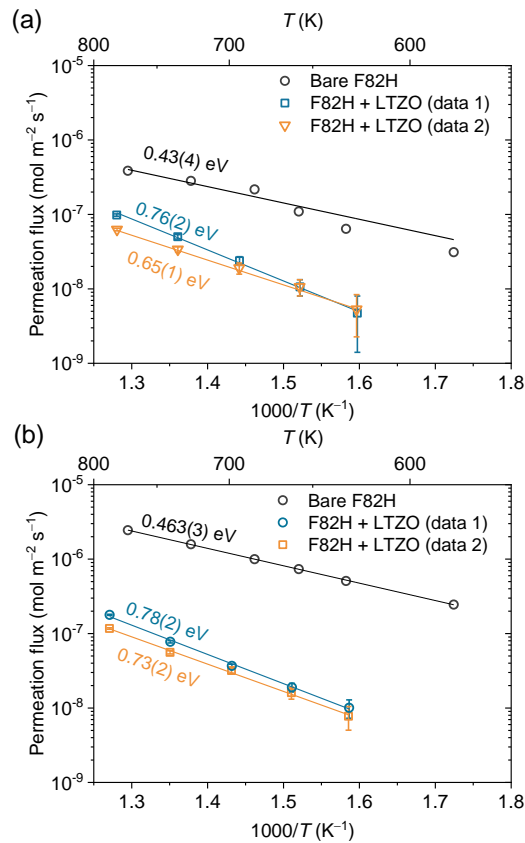


Fig. 4 Hydrogen permeation fluxes through the bare and corroded F82H samples under (a) Ar +0.1%$H_2$ and (b) Ar + 1.0% $H_2$ gas flow conditions. Numbers in unit of eV represent activation energies for the hydrogen permeation.

## 3.2 Material characterizations

The surface images of the F82H samples (upper side) after the permeation tests are displayed in Fig. 5. In Fig. 5a,b, spherical traces with diameters ranging from 200 to 300 µm were observed in the contact area on the F82H sample. The outer part of the F82H sample positioned outside of the double tube (see Fig. 1) became black and dark red due to oxidation in air. The surface image observed by the optical microscope showed that some central parts of the spherical traces were removed (white arrows in Fig. 5c). The central area of the spherical trace was the contact area of the LTZO pebbles and F82H, which presumably stuck together during the heating and separated each other when the pebbles were removed after the permeation tests. Fig. 5d shows the upper-side surface microstructure of the F82H tested under Ar + 1.0% $H_2$. The majority area of the F82H surface showed a dense microstructure of

the corroded area with crystal grains of ~1 µm without micropores (d1 in Fig. 5). This area corresponds to the non-contact area corroded by vapor gas from the pebbles. In contrast, the outer side of the sample oxidized in air showed a porous microstructure with needle-shaped crystal grains (d3 in Fig. 5). Formation of micro-sized particles was observed outside the solid-solid contact area, which may have been formed by exposure to a high concentration of the corrosive gas released from the pebbles (d2 in Fig. 5). The contacted area (d4 in Fig.5) had a similar microstructure to non-contacted area (d1 in Fig.5). Fig. 6 shows the cross-section SEM image and element mappings using energy-dispersive X-ray (EDX) spectrometer of the F82H sample (upper side) tested under Ar + 1.0% $H_2$ condition. Noted that Li was not detected due to its low emission energy of Li–$K\alpha$. The O mapping showed that the surface was covered by the oxidized layer. The thickness of the oxidized layer was $2.6 \pm 0.3$ µm. Segregations of Cr and Fe within the layer were not clearly observed from the EDX element mappings.
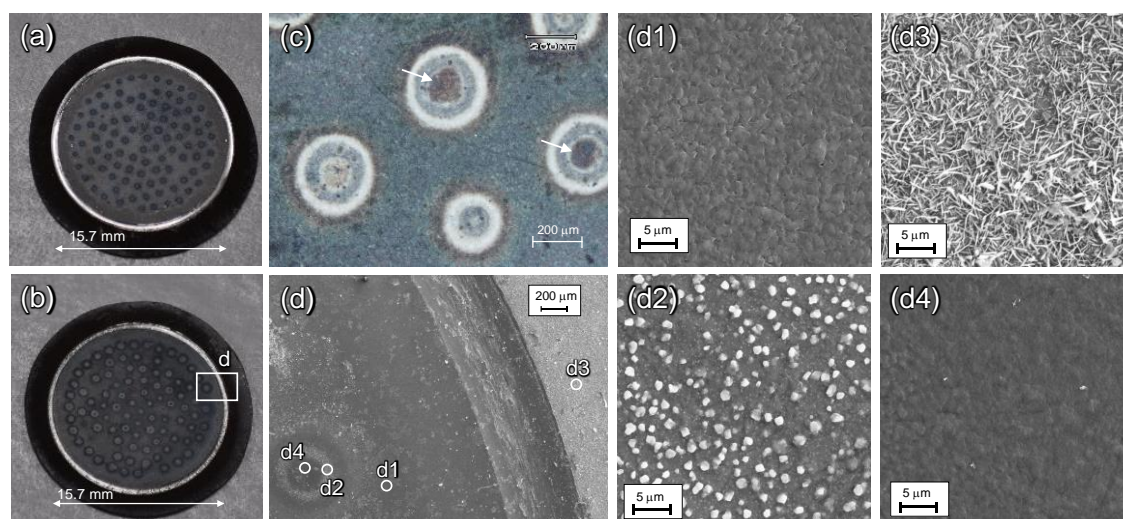


Fig. 5 Surface photos of the F82H sample (upper side) tested under (a) Ar + 0.1% $H_2$ and (b) Ar + 1.0% $H_2$ gas flow conditions. The F82H surface tested in Ar + 1.0% $H_2$ observed by (c) optical microscope and (d) scanning electron microscope (SEM). In panel (c), removed parts are represented with white arrows. Panel (d) shows (d1–4) positions.
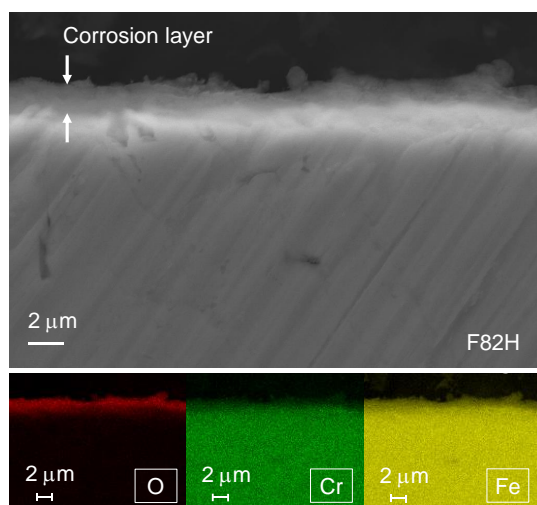
Fig. 6 Scanning electron microscope (SEM) image and energy-dispersive X-ray (EDX) element mappings of O, Cr, and Fe of the cross-section of the F82H sample (upper side) tested under Ar + 1.0% $H_2$ condition.

Fig. 7 and Fig. 8 show the element depth profiles obtained by GD-OES and XRD patterns, respectively. Two distinguishable layers on the F82H surface were observed in the GD-OES depth profiles (Fig. 7). The outer layer contained Li, Fe, O, and significantly low concentrations of Cr. The inner layer was composed of Li, Fe, Cr, and O. The thicknesses of the outer and inner layers were estimated to be ~0.85 and ~3.0 μm (Ar + 0.1% $H_2$) and ~0.35 and ~2 μm (Ar + 1.0% $H_2$). Based on the compositional information obtained by GD-OES, the peaks from the upper side of the F82H sample in contact with the LTZO pebbles were indexed as $LiCrO_2$ ($R\overline{3}m$), $LiFeO_2$ ($Fd\overline{3}m$), and $LiFe_5O_8$ ($P4_132$) phases. Trace peaks of the hematite phase ($Fe_2O_3$, space group: $R\overline{3}c$) were seen on both sides of the F82H samples. It is noted the compositions may not be exact because other Li–Cr–Fe–O phases such as $LiCrFe_4O_8$ ($Fd\overline{3}m$) have similar peak positions. In Fig. 7a, the depth profile of H indicated that the hydrogen concentration was mainly decreased in the outer layer. In contrast, the H concentration was decreased by both, the outer and inner layers, in the sample tested under Ar + 1.0% $H_2$, which could be explained by the fact the outer layer was not thick enough to reduce the higher H concentration at the surface. The H concentrations at the interface between the outer and inner layers showed a slight increase, indicating trapped H in microscopic defects at the interface. It is noteworthy that the results suggest that both layers have the ability to reduce hydrogen permeation.

The XRD patterns of the LTZO powders remained unchanged by the drying process and the permeation tests as shown in Fig. 8b. The patterns were indexed as a disordered cubic structure of $Li_2TiO_3$ with space group of $Fm\overline{3}m$ [38]. While no clear (002) peak of the 2C/c monoclinic structure ($2\theta$: ~22°), corresponding to the long-range ordering of the transition metal layers along the c axis (d spacing: ~4.87 Å) was detected, weak and broad humps were observed in the $2\theta$ range of 20–30°. This

indicates that the pebbles retained the disordered cubic structure even after the permeation test. Fig. 9 shows the pebbles as received, after drying at 623 K, and after the tests. The color of the pebbles after the test in Ar + 1.0% H$_2$ showed a slight change to light-gray. This color change could be caused by reduction of Ti (Ti$^{4+}$→Ti$^{3+}$) in the LTZO pebbles, originating from a narrowed band gap and enhanced absorption of visible light [39].
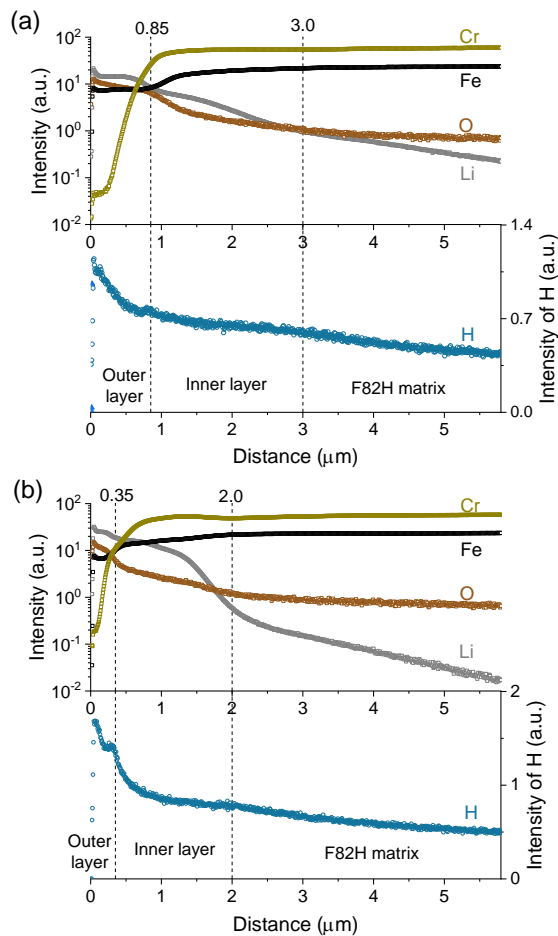


Fig. 7 Depth profiles in the F82H samples after the hydrogen permeation tests under (a) Ar + 0.1% H$_2$ and (b) Ar + 1.0% H$_2$ gas flow conditions using glow discharge optical emission spectroscopy (GD-OES).
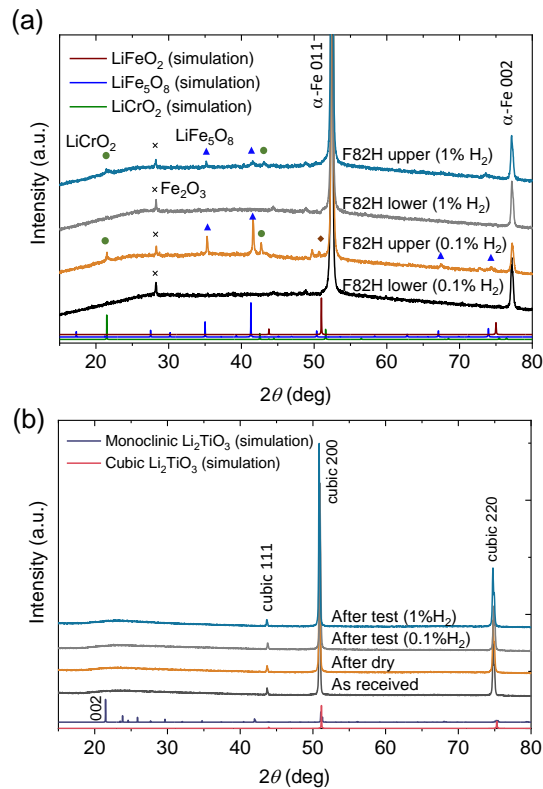
Fig. 8 X-ray diffraction (XRD) patterns using Co–Kα from (a) the F82H and (b) LTZO samples with the simulated patterns.
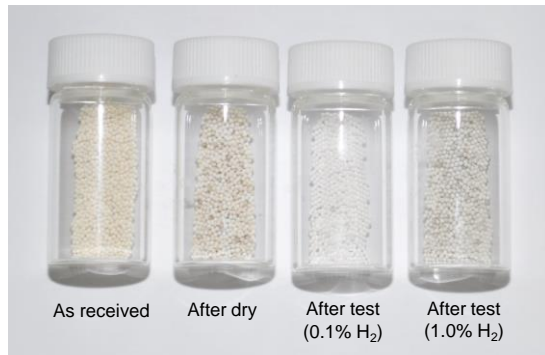


Fig. 9 Photo of the LTZO pebbles as received, after drying, and after the tests under the Ar + 0.1% $H_2$ and Ar + 1.0% $H_2$ conditions.

## 3.3 Discussion

In a breeding blanket of a fusion reactor, an RAFM structural steel material is in contact with breeder pebbles at elevated temperatures as high as the coolant temperature; i.e., 598 K for a water-cooled blanket [1]. By extrapolating the data in Fig. 4, the PRFs at 598 K of the corrosion layer formed under Ar + 0.1% $H_2$ gas flow condition were estimated to be 25 (data1) and 20 (data2), while those

under Ar + 1.0% H$_2$ condition were 45 (data1) and 50 (data2). The obtained PRFs were much higher than those of the thin Fe$_2$O$_3$/Cr$_2$O$_3$ oxidized layers formed on stainless steels by oxidation (PRF: 2–3) [40]. The high PRF values of the corrosion layers can be explained by not only the thickness but also the dense microstructure of the corrosion product compared to that formed by oxidation as observed in Fig. 5. Based on a previous study, the effective diffusion coefficient of oxygen ions into the corrosion layer exponentially decreases with inverse temperature [24], hence the thickness of the corrosion layers at 773 K is predicted to be 20 times greater than those at 598 K. This means that the heat treatment at 773 K for a total of 9 days performed in this study is equivalent to a heating for 180 days at 598 K. As a blanket will be used for 2–5 years of an operational period, the corrosion layer could be even thicker in a fusion environment.

The corrosion layers showed not only the ability to prevent hydrogen permeation but also thermal stability against temperature changes ($T_h$ = 623–773 K) as shown in Fig. 3. The good thermal stability can be explained by the thermal expansion compatibility between the substrate and corrosion layers. The thermal expansion coefficient of LiFe$_5$O$_8$ is 12.0 × 10$^{-6}$ K$^{-1}$ [41] that matches well with that of F82H (11.5 × 10$^{-6}$ K$^{-1}$) [42]. Although no thermal expansion coefficient of LiCrO$_2$ was found in the literature, the values of NaCrO$_2$ (LiCrO$_2$ type structure with the $R\bar{3}m$ space group) along the $x$ and $z$ directions are 9.0 × 10$^{-6}$ K$^{-1}$ and 14.8 × 10$^{-6}$ K$^{-1}$ [43], respectively, and similar to F82H. Moreover, the surface corrosion layers form spontaneously inside a breeding blanket, thus it is a cost-free permeation barrier which has a possible self-repairing ability; even cracks initiated in the corrosion layers by thermal stress, fresh metallic surface is immediately oxidized by the corrosive gas species, which consequently prevents fast hydrogen permeation. This ability would be promising for the fusion application, because a slip of ceramic breeder pebbles can scratch RAFM steel surface in a breeding blanket [44]. The self-repairing ability will be further investigated in our future work. One concern is the decline in the permeation reduction performance due to neutron irradiation, because the layers contain Li and thus produces tritium by neutron capture within the layers. An increase of tritium concentration and exothermic heat produced within the layers may have an influence on the hydrogen permeation properties.


## 4. Conclusions

Hydrogen permeation from a ceramic breeder pebble bed was measured to assess the effect of surface corrosion of a reduced activation ferritic martensitic (RAFM) F82H steel. The release of corrosive gas from the pebbles resulted in the formation of corrosion layers on the F82H sample with a dense surface microstructure, unlike a porous microstructure caused by oxidation in air without the pebbles. The permeation tests demonstrate that hydrogen permeation flux through an RAFM steel sample with no coating is suppressed by the corrosion layers at least by one order of magnitude. The

activation energies of hydrogen permeation through the corroded F82H steel were 0.65–0.78 eV, which are comparable with typical oxide coatings. The hydrogen depth profiles in the corroded sample showed that both of the Li–Fe–O outer and Li–Fe–Cr–O inner layers had the ability to reduce the permeation. The spontaneously formed layers had a good thermal stability against the temperature change at 623–773 K. These results suggest that the corrosion layer can serve as a cost-free hydrogen permeation barrier.

## Acknowledgement

## Declaration of competing interest

The authors declare that they have no competing financial interest.

## References

[1]     Konishi S, Enoeda M, Nakamichi M, Hoshino T, Ying A, Sharafat S, et al. Functional materials for breeding blankets—status and developments. Nucl Fusion 2017;57:092014. https://doi.org/10.1088/1741-4326/aa7e4e.

[2]     Hernández FA, Pereslavtsev P, Zhou G, Neuberger H, Rey J, Kang Q, et al. An enhanced, near-term HCPB design as driver blanket for the EU DEMO. Fusion Eng Des 2019;146:1186–91. https://doi.org/10.1016/j.fusengdes.2019.02.037.

[3]     Katayama K, Someya Y, Tobita K, Nakamura H, Tanigawa H, Nakamura M, et al. Estimation of tritium permeation rate to cooling water in fusion DEMO condition. Fusion Sci Technol 2017;71:261–7. https://doi.org/10.1080/15361055.2017.1288423.

[4]     Zajec B. Hydrogen permeation barrier - Recognition of defective barrier film from transient permeation rate. Int J Hydrogen Energy 2011;36:7353–61. https://doi.org/10.1016/j.ijhydene.2011.03.068.

[5]     Li Q, Liu J, Lv WL, Mo L Bin, Duan DW, Gu HW, et al. Stability of Y2O3 hydrogen isotope permeation barriers in hydrogen at high temperatures. Int J Hydrogen Energy 2013;38:4266–71. https://doi.org/10.1016/j.ijhydene.2013.01.110.

[6]     He D, Li S, Liu X, Zhang C, Yu Q, Lei Y, et al. Influence of microstructure on the hydrogen

permeation of alumina coatings. Int J Hydrogen Energy 2013;38:9343–8. https://doi.org/10.1016/j.ijhydene.2013.05.065.

[7]     Nemanič V. Hydrogen permeation barriers: Basic requirements, materials selection, deposition methods, and quality evaluation. Nucl Mater Energy 2019;19:451–7. https://doi.org/10.1016/j.nme.2019.04.001.

[8]     Zhang M, Zhao R, Ling Y, Wang R, Zhou Q, Wang J, et al. Preparation of Cr2O3/Al2O3 bipolar oxides as hydrogen permeation barriers by selective oxide removal on SS and atomic layer deposition. Int J Hydrogen Energy 2019;44:12277–87. https://doi.org/10.1016/j.ijhydene.2019.03.086.

[9]     Luo B, Bai P, An T, Zhang S, Wen X, Chen L, et al. Vapor-deposited iron sulfide films as a novel hydrogen permeation barrier for steel: Deposition condition, defect effect, and hydrogen diffusion mechanism. Int J Hydrogen Energy 2018;43:15564–74. https://doi.org/10.1016/j.ijhydene.2018.06.042.

[10]    Li Q, Mo L Bin, Wang J, Yan K, Tang T, Rao YC, et al. Performances of Cr2O3-hydrogen isotopes permeation barriers. Int J Hydrogen Energy 2015;40:6459–64. https://doi.org/10.1016/j.ijhydene.2015.03.093.

[11]    Forcey KS, Perujo A, Reiter F, Lolli-Ceroni PL. The formation of tritium permeation barriers by CVD. J Nucl Mater 1993;200:417–20. https://doi.org/doi.org/10.1016/0022-3115(93)90319-T.

[12]    Tamura M, Noma M, Yamashita M. Characteristic change of hydrogen permeation in stainless steel plate by BN coating. Surf Coatings Technol 2014;260:148–54. https://doi.org/10.1016/j.surfcoat.2014.09.041.

[13]    Hatano Y, Zhang K, Hashizume K. Fabrication of ZrO2 coatings on ferritic steel by wet-chemical methods as a tritium permeation barrier. Phys Scr T 2011;T145. https://doi.org/10.1088/0031-8949/2011/T145/014044.

[14]    Levchuk D, Koch F, Maier H, Bolt H. Deuterium permeation through Eurofer and α-alumina coated Eurofer. J Nucl Mater 2004;328:103–6. https://doi.org/10.1016/j.jnucmat.2004.03.008.

[15]    Engels J, Houben A, Linsmeier C. Hydrogen isotope permeation through yttria coatings on Eurofer in the diffusion limited regime. Int J Hydrogen Energy 2021;46:13142–9. https://doi.org/10.1016/j.ijhydene.2021.01.072.

[16]    Chikada T, Suzuki A, Adelhelm C, Terai T, Muroga T. Surface behaviour in deuterium permeation through erbium oxide coatings. Nucl Fusion 2011;51. https://doi.org/10.1088/0029-5515/51/6/063023.

[17]    Matějíček J, Veverka J, Nemanič V, Cvrček L, Lukáč F, Havránek V, et al. Characterization of less common nitrides as potential permeation barriers. Fusion Eng Des 2019;139:74–80. https://doi.org/10.1016/j.fusengdes.2018.12.056.

[18]    Hu L, Wei G, Yin R, Hong M, Cheng T, Zhang D, et al. Significant hydrogen isotopes

permeation resistance via nitride nano-multilayer coating. Int J Hydrogen Energy 2020;45:19583–9. https://doi.org/10.1016/j.ijhydene.2020.05.123.

[19]     Endoh R, Nogami S, Hishinuma Y, Chikada T. Submicron-thick yttria-stabilized zirconia coating as an advanced tritium permeation barrier. Nucl Fusion 2021;in press. https://doi.org/10.1088/1741-4326/ac044d.

[20]     Hernández T, Gázquez MC, Sánchez FJ, Malo M. Corrosion mechanisms of Eurofer produced by lithium ceramics under fusion relevant conditions. Nucl Mater Energy 2018;15:110–4. https://doi.org/10.1016/j.nme.2018.03.005.

[21]     Cho S, Park YH, Chun YB, Min KM, Ahn MY, Park SC, et al. Chemical compatibility between ARAA alloy and lithium meta-titanate breeder material. Fusion Eng Des 2017;124:1052–8. https://doi.org/10.1016/j.fusengdes.2017.04.007.

[22]     Mukai K, Sanchez F, Knitter R. Chemical compatibility study between ceramic breeder and EUROFER97 steel for HCPB-DEMO blanket. J Nucl Mater 2017;488:196–203. https://doi.org/10.1016/j.jnucmat.2017.03.018.

[23]     Mukai K, Gonzalez M, Knitter R. Effect of moisture in sweep gas on chemical compatibility between ceramic breeder and EUROFER97. Fusion Eng Des 2017;125:154–9. https://doi.org/10.1016/j.fusengdes.2017.10.001.

[24]     Mukai K, Sanchez F, Hoshino T, Knitter R. Corrosion characteristics of reduced activation ferritic-martensitic steel EUROFER by Li2TiO3 with excess Li. Nucl Mater Energy 2018;15:190–4. https://doi.org/10.1016/j.nme.2018.04.010.

[25]     Aktaa J, Walter M, Gaisina E, Kolb MHH, Knitter R. Assessment of the chemical compatibility between EUROFER and ceramic breeder with respect to fatigue lifetime. Fusion Eng Des 2020;157:111732. https://doi.org/10.1016/j.fusengdes.2020.111732.

[26]     Zhang W, Zhu C, Yang J, Chen Q, Wang L, Feng Y, et al. Chemical compatibility between the α-Al2O3 tritium permeation barrier and Li4SiO4 tritium breeder. Surf Coatings Technol 2021;410:126960. https://doi.org/10.1016/j.surfcoat.2021.126960.

[27]     Chikada T, Kolb MHH, Fujita H, Nakamura K, Kimura K, Rasinski M, et al. Compatibility of tritium permeation barrier coatings with ceramic breeder pebbles. Corros Sci 2021;182:109288. https://doi.org/10.1016/j.corsci.2021.109288.

[28]     Kimura K, Mochizuki J, Horikoshi S, Matsunaga M, Fujita H, Okitsu K, et al. Oxide layer formation in reduced activation ferritic steel F82H under DEMO reactor blanket condition. Fusion Eng Des 2019;146:1564–8. https://doi.org/10.1016/j.fusengdes.2019.02.129.

[29]     Wang L, Ye X, Feng Y, Luo X, Hong Z, Yan J, et al. Hydrogen isotope permeability of reduced activation ferritic/martensitic steel CLF-1 corroded by Li4SiO4. Fusion Eng Des 2020;153:111490. https://doi.org/10.1016/j.fusengdes.2020.111490.

[30]     Tanigawa H, Shiba K, Sakasegawa H, Hirose T, Jitsukawa S. Technical issues related to the

development of reduced-activation ferritic/martensitic steels as structural materials for a fusion blanket system. Fusion Eng Des 2011;86:2549–52. https://doi.org/10.1016/j.fusengdes.2011.04.047.

[31]  Sakasegawa H, Tanigawa H, Kano S, Enomoto M. Precipitation behavior in F82H during heat treatments of blanket fabrication. Fusion Eng Des 2011;86:2541–4. https://doi.org/10.1016/j.fusengdes.2011.03.087.

[32]  Hoshino T. Pebble fabrication of super advanced tritium breeders using a solid solution of Li2+xTiO3+y with Li2ZrO3. Nucl Mater Energy 2016;9:221–6. https://doi.org/10.1016/j.nme.2016.05.004.

[33]  Momma K, Izumi F. VESTA 3 for three-dimensional visualization of crystal, volumetric and morphology data. J Appl Crystallogr 2011;44:1272–6. https://doi.org/10.1107/S0021889811038970.

[34]  Kulsartov T V., Hayashi K, Nakamichi M, Afanasyev SE, Shestakov VP, Chikhray Y V., et al. Investigation of hydrogen isotope permeation through F82H steel with and without a ceramic coating of Cr2O3-SiO2 including CrPO4 (out-of-pile tests). Fusion Eng Des 2006;81 A:701–5. https://doi.org/10.1016/j.fusengdes.2005.07.019.

[35]  Dolinsky YN, Zouev YN, Lyasota IA, Saprykin I V., Sagaradze V V. Permeation of deuterium and tritium through the martensitic steel F82H. J Nucl Mater 2002;307–311:1484–7. https://doi.org/10.1016/S0022-3115(02)01128-5.

[36]  Byeon WJ, Lee SK, Noh SJ. Transport of hydrogen and deuterium in 316LN stainless steel over a wide temperature range for nuclear hydrogen and nuclear fusion applications. Int J Hydrogen Energy 2020;45:8827–32. https://doi.org/10.1016/j.ijhydene.2020.01.130.

[37]  Mukai K, Yasumoto M, Terai T. Lithium Vapor Chemistry of Hyper-Stoichiometric Lithium Metatitanate Li2.12(2)TiO3+y. J Phys Chem C 2020;124:10870–7. https://doi.org/10.1021/acs.jpcc.0c02454.

[38]  Laumann A, Fehr KT, Boysen H, Hoelzel M, Holzapfel M. Temperature-dependent structural transformations of hydrothermally synthesized cubic Li2TiO3 studied by in-situ neutron diffraction. Zeitschrift Fur Krist 2011;226:53–61. https://doi.org/10.1524/zkri.2011.1286.

[39]  Tan H, Zhao Z, Niu M, Mao C, Cao D, Cheng D, et al. A facile and versatile method for preparation of colored TiO2 with enhanced solar-driven photocatalytic activity. Nanoscale 2014;6:10216–23. https://doi.org/10.1039/c4nr02677b.

[40]  Ishikawa Y, Yoshimura T, Arai M. Effect of surface oxide layers on deuterium permeation through stainless steels with reference to outgassing reduction in ultra- to extremely high vacuum. Vacuum 1996;47:357–61. https://doi.org/10.1016/0042-207X(95)00251-0.

[41]  Kato E. Phase Transition of Li2O–Fe2O3 System. II. Thermal and Electric Properties of Lithium Ferrospinel LiFe5O8. Bull Chem Soc Jpn 1958;31:113–7. https://doi.org/10.1246/bcsj.31.113.

[42]    Hirose T, Nozawa T, Stoller RE, Hamaguchi D, Sakasegawa H, Tanigawa H, et al. Physical properties of F82H for fusion blanket design. Fusion Eng Des 2014;89:1595–9. https://doi.org/10.1016/j.fusengdes.2013.12.005.

[43]    Yabuuchi N, Ikeuchi I, Kubota K, Komaba S. Thermal Stability of NaxCrO2 for Rechargeable Sodium Batteries; Studies by High-Temperature Synchrotron X-ray Diffraction. ACS Appl Mater Interfaces 2016;8:32292–9. https://doi.org/10.1021/acsami.6b09280.

[44]    Takahashi N, Kondo M, Kim J-H, Nakamichi M. Fundamental Study on Fretting Corrosion in Solid Breeder Blanket. Plasma Fusion Res 2021;16:2405032. https://doi.org/10.1585/pfr.16.2405032.